

Self-gating in semiconductor electrocatalysis

Yongmin He^{1,2,13}, Qiyuan He^{1,13}, Luqing Wang³, Chao Zhu¹, Prafful Golani¹, Albertus D. Handoko⁴, Xuechao Yu², Caitian Gao², Mengning Ding⁵, Xuewen Wang¹, Fucui Liu⁶, Qingsheng Zeng¹, Peng Yu¹, Shasha Guo¹, Boris I. Yakobson³, Liang Wang⁷, Zhi Wei Seh⁴, Zhuhua Zhang⁸, Minghong Wu⁷, Qi Jie Wang^{2,9*}, Hua Zhang^{1,10*} and Zheng Liu^{1,9,11,12*}

The semiconductor–electrolyte interface dominates the behaviours of semiconductor electrocatalysis, which has been modelled as a Schottky-analogue junction according to classical electron transfer theories. However, this model cannot be used to explain the extremely high carrier accumulations in ultrathin semiconductor catalysis observed in our work. Inspired by the recently developed ion-controlled electronics, we revisit the semiconductor–electrolyte interface and unravel a universal self-gating phenomenon through microcell-based in situ electronic/electrochemical measurements to clarify the electronic-conduction modulation of semiconductors during the electrocatalytic reaction. We then demonstrate that the type of semiconductor catalyst strongly correlates with their electrocatalysis; that is, n-type semiconductor catalysts favour cathodic reactions such as the hydrogen evolution reaction, p-type ones prefer anodic reactions such as the oxygen evolution reaction and bipolar ones tend to perform both anodic and cathodic reactions. Our study provides new insight into the electronic origin of the semiconductor–electrolyte interface during electrocatalysis, paving the way for designing high-performance semiconductor catalysts.

The semiconductor–electrolyte interface governs semiconductor electrocatalytic behaviour^{1–4}. In fundamental electrochemistry, the Schottky-analogue junction is used to model charge transfer kinetics across the interface during electrochemical reactions^{5–7}, with classical electron transfer theories (for example, Marcus theory⁸ and the Gerischer model⁹). In such a case, the charge transfer process is determined by the band alignment between the semiconductor and the redox species, and the interface is considered fully active for this process. Meanwhile, from an electronics point of view, a metal–insulator–semiconductor (MIS) junction is used to describe the semiconductor–electrolyte interface, especially for charge-transport modulation, in the emerging field of ion-controlled electronics (ionic gating or electrochemical gating)^{10–14}. In this case, the interface is considered fully inert without the charge transfer process, and is thus capable of accumulating an extremely high surface charge concentration (exceeding 10^{14} ecm⁻²) with an ultrahigh electric field (on the order of 10 MV cm⁻¹), making the semiconductor highly conductive^{10,11} or even superconductive^{15,16}.

Recent works suggest that the semiconductor electrocatalytic surface can be considered as a mixture of ‘active’ and ‘inert’ regions, and the charge transfer process mainly occurs at certain active crystal planes in bulk materials^{17–19} or at atomically active sites (for example, defects or edges) in ultrathin materials^{20–22}. Unfortunately, such a mixed interface cannot be well described by the Schottky-analogue junction or the MIS junction.

Here, by using microcell-based in situ electronic/electrochemical measurements, we find that the electrocatalytic reaction itself can strongly modulate the surface conductance of semiconductor electrocatalysts in a process defined as self-gating. As a consequence, the surface can be modulated to be highly conductive (‘on’) or insulating (‘off’), strongly correlating with the electrocatalytic reactions. The self-gating phenomenon can explain why ultrathin semiconductors can be used as highly efficient electrocatalysts, although semiconductors have been predicted to be non-ideal catalysts due to their low intrinsic carrier concentration²³. Importantly, our experiments suggest that the self-gating phenomenon could universally exist in various semiconductors, including two-dimensional (2D) transition metal dichalcogenides (TMDs) and 1D Si nanowires.

In our experiment, a four-electrode microcell (Fig. 1a and Supplementary Figs. 1 and 2)^{24,25} was used to simultaneously collect the electronic and electrochemical signals of semiconductor electrocatalysts (that is, in situ electronic/electrochemical measurements) and ultrathin TMD nanosheets^{20,22} were used as semiconductor electrocatalysts. Figure 1b presents an optical image of the fabricated microcell. The overall set-up is shown in Fig. 1b(i), and the micro-electrochemical environment and the device are shown in Fig. 1b(ii) and (iii), respectively. Spatial control of the electrocatalytic reaction was achieved by carving a small window in a passive poly(methylmethacrylate) (PMMA) layer, ensuring that the reaction only occurred on the region of interest (Supplementary Fig. 3).

¹School of Materials Science and Engineering, Nanyang Technological University, Singapore, Singapore. ²Center for OptoElectronics and Biophotonics, School of Electrical and Electronic Engineering & The Photonics Institute, Nanyang Technological University, Singapore, Singapore. ³Department of Materials Science and NanoEngineering, Rice University, Houston, TX, USA. ⁴Institute of Materials Research and Engineering, Agency for Science, Technology and Research (A*STAR), Singapore, Singapore. ⁵Key Laboratory of Mesoscopic Chemistry of MOE, School of Chemistry and Chemical Engineering, Nanjing University, Nanjing, China. ⁶School of Optoelectronic Science and Engineering, University of Electronic Science and Technology of China, Chengdu, China. ⁷School of Environmental and Chemical Engineering, Shanghai University, Shanghai, China. ⁸State Key Laboratory of Mechanics and Control of Mechanical Structures, and Institute of Nanoscience, Nanjing University of Aeronautics and Astronautics, Nanjing, China. ⁹CINTRA CNRS/NTU/THALES, Research Techno Plaza, Singapore, Singapore. ¹⁰Department of Chemistry, City University of Hong Kong, Kowloon, Hong Kong, China. ¹¹School of Electrical and Electronic Engineering, Nanyang Technological University, Singapore, Singapore. ¹²Environmental Chemistry and Materials Centre, Nanyang Environment and Water Research Institute, Singapore, Singapore. ¹³These authors contributed equally: Yongmin He, Qiyuan He *e-mail: qjwang@ntu.edu.sg; HZhang@ntu.edu.sg; hua.zhang@cityu.edu.hk; z.liu@ntu.edu.sg

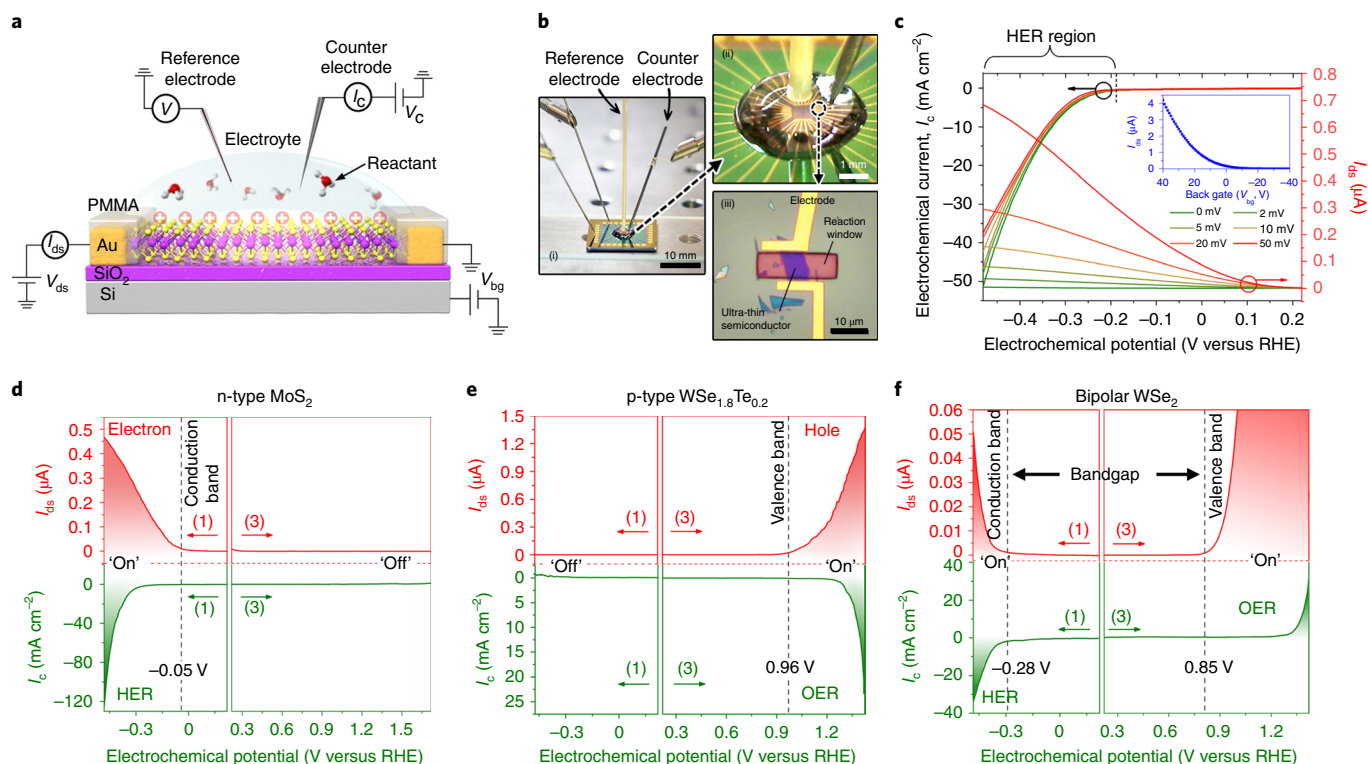


Fig. 1 | Demonstration of the self-gating phenomenon by in situ electronic/electrochemical measurements. **a**, Schematic of the microcell-based in situ electronic/electrochemical measurements. Both the electronic signal (I_{ds} , conductance current) and electrochemical signal (I_c , reaction current) of the TMD nanosheet can be collected simultaneously. Before the in situ electronic/electrochemical measurements, the type of majority charge carrier for each device is pre-identified by a back-gated measurement (V_{bg}) on the SiO₂ (285 nm)/Si substrate. **b**, Optical image of the microcell: overall set-up with four electrodes (i), enlarged view of the electrolyte (0.5 M H₂SO₄) droplet in which the reaction occurs (ii) and the mechanically exfoliated TMD device with a micro-sized reaction window in the PMMA passivation (iii). **c**, Typical electrochemical (I_c , y axis in black) and electronic (I_{ds} , y axis in red) signals of single-layer WS₂ during the HER at different bias potentials (V_{ds} : 0, 2, 5, 10, 20 and 50 mV), showing the self-gating phenomenon. Inset, back-gated measurements on the same device. Note that I_{ds} is normally 10–1,000 times I_c . **d–f**, In situ electronic/electrochemical measurements of three types of semiconductor electrocatalyst, including n-type MoS₂ (**d**), p-type WSe_{1.8}Te_{0.2} (**e**) and bipolar WSe₂ (**f**). Red curves in the top panels are obtained from the electronic measurements, and green curves in the bottom panels are obtained from the electrochemical measurements. Arrows indicate the scan directions of the electrochemical potential (see scans 1 and 3 in Supplementary Fig. 5 for details). Note, given that a large bias voltage would compromise the electrochemical potential, the bias voltage in our experiments was kept at 50 mV to collect electronic signals and ensure minimal interference with the electrochemical signals. In **d**, n-type MoS₂ is turned on at a negative electrochemical potential and only delivers the HER. In **e**, p-type WSe_{1.8}Te_{0.2} is turned on at a positive electrochemical potential and only delivers the OER. In **f**, bipolar WSe₂ is turned on at both negative and positive electrochemical potentials and can deliver the HER and OER, respectively. Accordingly, the Fermi level is tuned to the band edges of the conduction band and the valence band, respectively, experimentally identifying the bandgap.

Detailed information about the calibration and measurements of the microcell is provided in Supplementary Figs. 4–6.

Using the fabricated microcell, we first conducted in situ electronic/electrochemical measurements on a single-layer WS₂ nanosheet with a thickness of 6.5 Å. Figure 1c presents the electrochemical (polarization curves, black y axis) and electronic (conductance curves, red y axis) measurements during the hydrogen evolution reaction (HER) at various drain–source voltages (V_{ds} , 0–50 mV). In the electrochemical measurements, the HER performance (onset potential of approximately –208 mV versus the reversible hydrogen electrode (RHE) and a Tafel slope of ~108 mV dec⁻¹; see Supplementary Fig. 7) is comparable with that of the previously reported single-layer WS₂ (refs. 22,26). In the electronic measurements, the drain–source current (I_{ds}) shows an on/off ratio of 10⁴ (V_{ds} = 50 mV) and a very small saturation potential (approximately –0.4 V versus RHE), indicating an efficient conductance modulation of single-layer WS₂ during the HER. These electronic transport results closely resemble a typical ionic-gating transistor^{11,27} with n-type semiconducting characteristics, as demonstrated by back-gated

measurements on the same device (inset, Fig. 1c). In a classic field-effect transistor (FET), the conductance modulation is realized through the gate electrode^{11,27,28}. However, in our experiment, the conductance modulation relies on the electrochemical potential itself, without any additional gate electrode. Therefore, we term this phenomenon self-gating. The gating strength is expressed as $\Delta V_G = \Delta E_f/e + \Delta\phi$ (refs. 29,30), where ΔV_G is the change in gate voltage (that is, the inverse value of the electrochemical potential), ΔE_f is the change in chemical potential (Fermi level), e is the elementary charge and $\Delta\phi$ is the change in electrostatic potential. In an aqueous electrolyte (0.5 M H₂SO₄), $e\Delta V_G \approx \Delta E_f$ is obtained (see detailed calculation in Supplementary Note 1), suggesting an effective tuning of the semiconductor's Fermi level during electrocatalysis.

Importantly, the self-gating phenomenon is valid for a variety of ultrathin semiconductor catalysts. Figure 1d–f shows the electronic signals (upper panels, red curves) and electrochemical signals (lower panels, green curves) of three types of semiconducting TMD with different majority charge carriers (electrons, holes and both). In the electronic measurements, MoS₂, an n-type semiconductor, shows a

threshold voltage of -50 mV (versus RHE) and an on/off ratio of 5×10^3 (Fig. 1d). As a p-type semiconductor, $\text{WSe}_{1.8}\text{Te}_{0.2}$ shows a threshold voltage of 960 mV (versus RHE) and an on/off ratio of over 1×10^4 (Fig. 1e). Clearly, the bipolar WSe_2 shows two threshold voltages, at each polarity (Fig. 1f). Back-gated measurements on the same devices further proved their semiconducting characteristics (n-type for MoS_2 , p-type for $\text{WSe}_{1.8}\text{Te}_{0.2}$ and bipolar for WSe_2), as shown in Supplementary Fig. 8. Interestingly, in our experiment, the bandgap of bipolar WSe_2 (~ 1.13 eV, Supplementary Note 2) can be directly extracted from the electronic characteristics in Fig. 1f, and it aligns well with reported values (1.10 – 1.30 eV)²⁸, experimentally confirming effective tuning of the Fermi level ($e\Delta V_G \approx \Delta E_F$)—that is, self-gating. This is also confirmed by the observed low sub-threshold swing, 68 mV dec^{-1} (Supplementary Fig. 9), which is close to the ideal value (60 mV dec^{-1} at room temperature) in electronic measurements^{30,31}. Moreover, we also observed this kind of gating phenomenon in other semiconducting TMD catalysts, such as ReS_2 (Supplementary Fig. 10), PtSe_2 (Supplementary Fig. 11) and MoTe_2 (Supplementary Fig. 12), and also in different electrolyte conditions, such as salt and buffer solutions (Supplementary Fig. 13).

The lower panels of Fig. 1d–f show the electrochemical measurements of n-type MoS_2 , p-type $\text{WSe}_{1.8}\text{Te}_{0.2}$ and bipolar WSe_2 , and their corresponding Tafel plots are shown in Supplementary Fig. 14. The n-type MoS_2 is turned on by self-gating at a negative potential of -0.05 V (versus RHE) and delivers a high conductance, for example, 2.60 Ωmm at -0.19 V (versus RHE) and 0.61 Ωmm at -0.48 V (versus RHE), thus showing HER activity (Fig. 1d and Supplementary Fig. 14a). At a positive potential, MoS_2 is turned off with a low conductance ($\sim 2,975.6$ Ωmm) and shows no electrochemical activity. In comparison, p-type $\text{WSe}_{1.8}\text{Te}_{0.2}$ is turned on at a positive potential of 0.96 V (versus RHE) and turned off at a negative potential, thus only exhibiting OER activity (Fig. 1e and Supplementary Fig. 14b). Meanwhile, bipolar WSe_2 can be turned on at both negative (-0.28 V versus RHE) and positive (0.85 V versus RHE) potentials, performing both HER and OER activities (Fig. 1f and Supplementary Fig. 14c,d). These results suggest that the electrochemical reactions can only occur when the ultrathin semiconductor catalysts are turned on by self-gating. Otherwise, they behave like an insulator, without any electrochemical reactions when turned off by self-gating. Under self-gating, the strong correlation between the semiconducting types and the suitable catalytic reactions can be applied to other semiconducting TMD catalysts, such as ReS_2 , PtSe_2 and MoTe_2 (Supplementary Figs. 10 and 12).

For electrochemistry analysis we carried out electrochemical impedance spectroscopy (EIS) measurements in our microcell (Fig. 1a and Supplementary Fig. 15) to identify self-gating on MoS_2 during the HER. As a control experiment, Au was also assessed (Supplementary Fig. 16). This showed a HER performance comparable to that of MoS_2 (Supplementary Fig. 17), representing a metal–electrolyte interface. Nyquist plots of Au and MoS_2 nanosheet microelectrodes at various electrochemical potentials in the HER are shown in Fig. 2a,d, respectively. Their corresponding Bode angle plots are shown in Fig. 2b,e, respectively. The EIS data for the Au electrode can fit an equivalent circuit containing parallel $R_{\text{ct}}/Q_{\text{edl}}$ elements (Fig. 2c), which can be interpreted as a Faradaic charge transfer process. Interestingly, the EIS data obtained from the MoS_2 nanosheet can fit two series equivalent circuits (Fig. 2f). The low-frequency element is similar to that of Au (Fig. 2c), while the high-frequency one can be fit into a parallel R/C equivalent circuit (blue circuit, Fig. 2f), indicating charge transport to the electrocatalytic interface. This step could be associated with the charge-transport resistance (R_{ct}) and quantum capacitance (C_q) for an ultrathin MoS_2 nanosheet^{32–34}. Both R_{ct} and C_q exhibit strong electrochemical potential dependence, as shown in Fig. 2g,h, respectively. R_{ct} increases with the electrochemical potential, which aligns well with the self-gating induced conductance decrease in the MoS_2 nanosheet, which

is an n-type semiconductor (Fig. 1d). Notably, R_{ct} directly extracted from the EIS (green, Fig. 2g) is comparable to the resistance (R) obtained from in situ electronic measurements (red in Fig. 2g and Supplementary Fig. 17b), indicating that our in situ electronic/electrochemical measurement is valid. C_q increases with negative electrochemical potential (Fig. 2h), indicating that the Fermi level is tuned deeper inside the conduction band of MoS_2 by self-gating, similar to the observations in top-gated FETs^{32,33}. In addition, there is no obvious change in the total capacitance (C_{total}) series-connected capacitors of C_q and C_{edl} across the whole semiconductor–electrolyte interface in the electrochemical potential range (Fig. 2i), suggesting quasi-stable self-gating during the electrocatalytic reaction.

The observed self-gating phenomenon is distinct from classic electron transfer theories. Current electron transfer theories^{1–4}, including Marcus theory and the Gerischer model, assume a fully active semiconductor–electrolyte interface that works as a Schottky-analogue junction, in which the majority carriers can be accumulated under the electrochemical potential. However, similar to junction field-effect transistors^{35,36}, it is difficult for such a junction to accumulate a high carrier concentration or achieve high conductivity—the Fermi level is deep inside the conduction or valence band—because the Schottky-analogue junction approaches ohmic characteristics once the charge transfer process (the electrochemical reaction) starts. On the other hand, the recently developed ion-controlled electronics assume a fully inert interface, which works as an ionic gating or MIS junction^{28,37}. Such ionic gating is capable of accumulating an extremely high charge concentration (exceeding 1×10^{14} e^-cm^{-2} in 2D semiconductors) to make the semiconductor conductive^{10,11} or even superconductive^{15,16}. However, as current electron transfer theories mainly focus on the active region and overlook the inert region, they cannot be used to explain the exceptionally high carrier accumulation observed in the present experiment. Based on our experiments on different types of semiconductor, we propose that, in terms of the carrier modulation, a practical semiconductor–electrolyte interface containing both active and inert regions can be modelled as a leakage MIS (LMIS) junction, that is, leakage ionic gating (see Supplementary Table 3 and Supplementary Figs. 18–20 for details). In this model, the leakage refers to the charge transfer process from the active region to the reactant, and MIS refers to the self-gating modulated surface conductance, which will be further discussed in the following.

The middle panel of Fig. 3a schematically illustrates a device comprising a 35-nm-thick MoS_2 flake with top and bottom electrodes (for device fabrication see Supplementary Fig. 21), where both surface and bulk conductance can be measured during the HER. A strong self-gating phenomenon is observed on the top-electrode device (left, Fig. 3a). However, weak conductance modulation is observed on the bottom-electrode device (right panel, Fig. 3a). That is, a high surface conductance is only observed at the top surface of the MoS_2 , resulting in higher HER activity compared to bulk MoS_2 , with its low conductance.

We next examined the penetration depth of the surface conductance in the device with a bottom electrode configuration (inset of Fig. 3b and Supplementary Fig. 22), where the electrochemical current transports vertically through the MoS_2 flake to the bottom electrode. Figure 3b shows the MoS_2 -thickness-dependent HER current density at -0.4 V versus RHE (for the polarization curves see Supplementary Fig. 23b). Obviously, 1 nm single-layer MoS_2 (see first image in Supplementary Fig. 22) shows the highest HER activity ($j_{\text{max}} \approx 150$ mA cm^{-2}). The current decays rapidly with MoS_2 thickness ($j/j_{\text{max}} = 50\%$ and 10% at 5 and 16 nm MoS_2 , respectively). When the MoS_2 thickness exceeds 40 nm, it does not show obvious HER activity. Here, we define the penetration depth at 1% of the max current (for example, $j/j_{\text{max}} = 1\%$), which is ~ 25 nm for MoS_2 in the HER. From the aspect of semiconducting electronics, the penetration depth of the surface conductance is determined by the

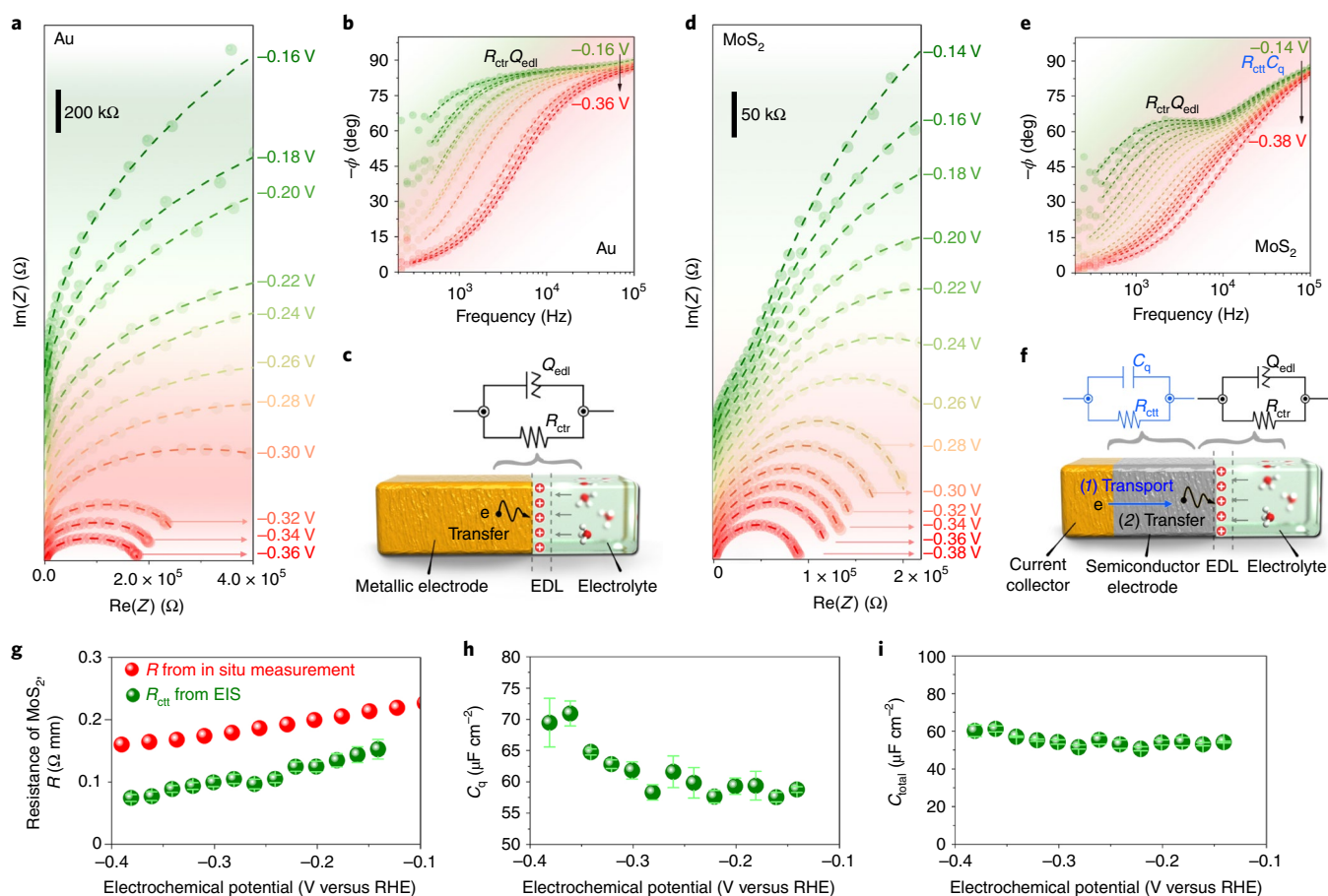


Fig. 2 | Demonstration of the self-gating phenomenon with EIS. a, b, Nyquist impedances (**a**) and Bode angle plot (**b**) of the Au microelectrode at various electrochemical potentials (20 mV per step) in the HER. **c,** Equivalent Randles circuits ($Q_{\text{edl}}/R_{\text{ctr}}$) of the Au microelectrode (see Supplementary Table 1 and Supplementary Fig. 15 for details), in which R_{ctr} and Q_{edl} are the charge transfer resistance and the constant-phase element related to the electrical double-layer (EDL) capacitance (C_{edl}), respectively. **d, e,** Nyquist impedances (**d**) and Bode angle plot (**e**) of the 8-nm-thick MoS₂ nanosheet microelectrode at various electrochemical potentials (20 mV per step) in the HER. **f,** Equivalent Randles circuits ($Q_q/R_{\text{ctt}} + Q_{\text{edl}}/R_{\text{ctr}}$) of the MoS₂ nanosheet microelectrode (see Supplementary Table 2 and Supplementary Fig. 16 for details), in which R_{ctt} and C_q are the charge-transport resistance and quantum capacitance, respectively. This Q_q/R_{ctt} circuit shows that the semiconductor electrode undergoes an additional step of charge transport to the electrocatalytic interface, compared to the metallic electrode. Dashed lines in **a, b, d, e** are the fitting results according to the respective Randles equivalent circuit. **g,** Consistency of the charge transport resistances of the MoS₂ nanosheet microelectrode measured in both in situ electronic measurements (R , red) and EIS measurements (R_{ctt} , green). **h,** Electrochemical potential-dependent C_q measured in the HER. **i,** Total capacitance (C_{total}) of the MoS₂ nanosheet microelectrode calculated based on the equation ($1/C_{\text{total}} = 1/C_{\text{edl}} + 1/C_q$), suggesting quasi-stable self-gating at the semiconductor–electrolyte interface.

carrier density in the accumulation regime under self-gating. Our theoretical calculations (Supplementary Note 4 and Supplementary Fig. 24) show that this depth is estimated to be on the scale of tens of nanometres beneath the semiconductor surface (Fig. 3c), in line with our experimental results.

To the best of our knowledge, the aforementioned surface conductance has not been investigated in semiconductor electrocatalysis. In our experiment, we found that self-gating could induce a charge transport pathway that renders the surface of semiconductors highly conductive (Fig. 3d). As a result, charge carriers can transport within the surface of the semiconductor instead of its bulk, which is different from a metallic electrocatalyst, where charge carriers transport through its highly conductive bulk (for a detailed discussion see Supplementary Note 5). Importantly, the concept of surface conductance can explain the high electrocatalytic activities of nanostructured semiconductor catalysts such as metal oxide^{38–41} and 2D metal dichalcogenides^{20,22,42}, because they can be effectively modulated into a highly conductive state once their thickness is within the accumulation regime. It can also explain the high activities of previously reported semiconductor

catalysts, even without conductive additives^{22,43,44}. Therefore, the surface conductance strongly correlates with the electrocatalytic activity of a semiconductor catalyst.

As shown in Fig. 4a, when the semiconductor catalyst is turned on under self-gating, its surface becomes conductive and the cathodic reaction takes place. Otherwise, its surface is insulated without electrocatalytic reactions (Fig. 4b). As a result, n-type semiconductor catalysts can be turned on by a negative electrochemical potential (positive gating), making them suitable for cathodic reactions, such as the HER and CO₂ reduction (Fig. 4c). Meanwhile, p-type semiconductor catalysts can be turned on by a positive electrochemical potential (negative gating), resulting in anodic reactions, such as the OER and oxygen reduction reaction (ORR). Bipolar semiconductor catalysts can be turned on by both positive and negative potentials, leading to anodic and cathodic reactions, respectively. This principle has been proved by our experiments on various materials, including 2D materials such as WS₂ (Fig. 1c), MoS₂ (Fig. 1d and Supplementary Fig. 17b), WSe₂ (Fig. 1f), ReS₂ (Supplementary Fig. 10), PtSe₂ (Supplementary Fig. 11), MoTe₂ (Supplementary Fig. 12) and WSe_{1.8}Te_{0.2} (Fig. 1e), conventional semiconductors such

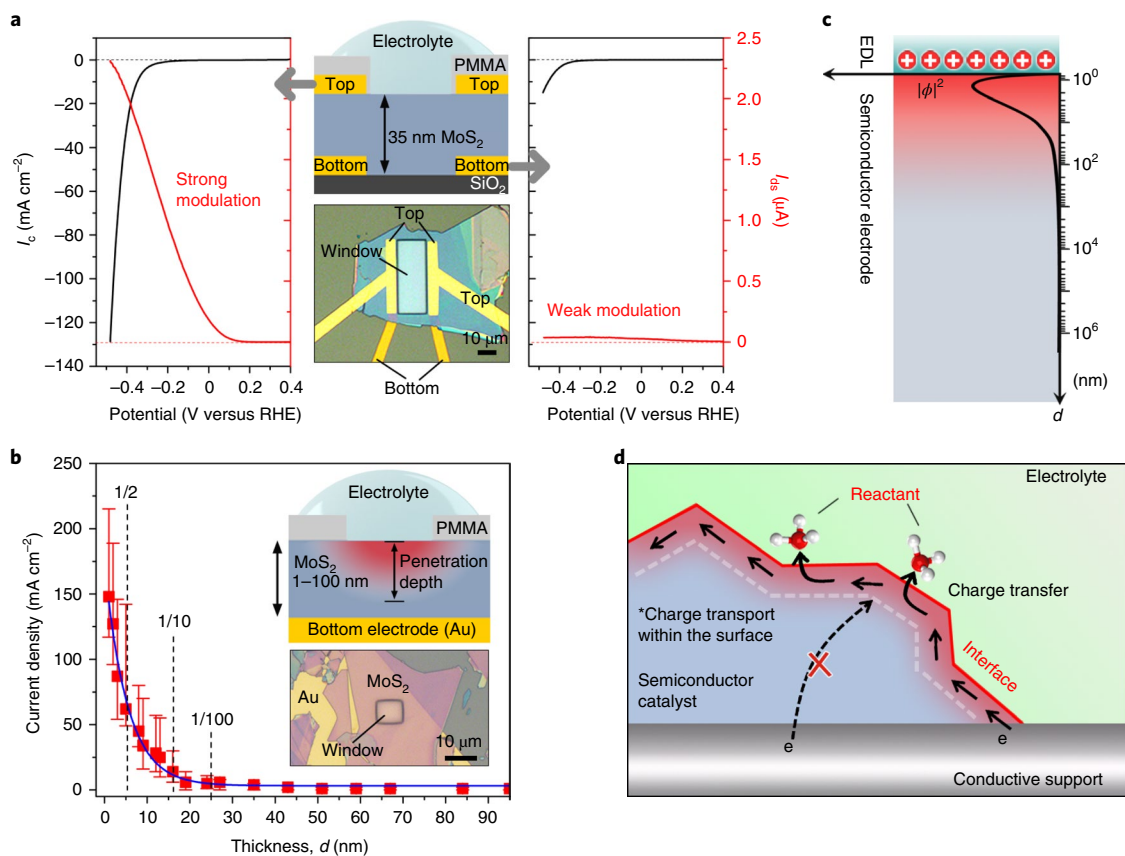


Fig. 3 | Self-gating modulated surface conductance of a semiconductor catalyst. **a**, In situ electronic/electrochemical measurements performed on a 35-nm-thick MoS₂ flake in a microcell with top (left panel) and bottom (right panel) electrodes. Middle panel, schematic of the microcell (top) and a corresponding optical microscopy image (bottom). **b**, The HER activity (current density) of the MoS₂ drops quickly as its thickness increases. Inset, schematic of the microcell with bottom electrode (top) and the corresponding optical microscopy image (bottom). **c**, Calculated carrier density as a function of the thickness of the semiconductor catalyst at the semiconductor–electrolyte interface under an electric field on the order of 10 MV cm⁻¹. A high carrier density is realized on the surface of the semiconductor electrode. **d**, Schematic of the surface conductance of the semiconductor electrocatalyst. A surface conductive pathway is formed when the surface of the semiconductor electrocatalyst is turned on by the electrochemical potential under self-gating, allowing charge transfer via the semiconductor–electrolyte interface—that is, the electrocatalytic reaction takes place.

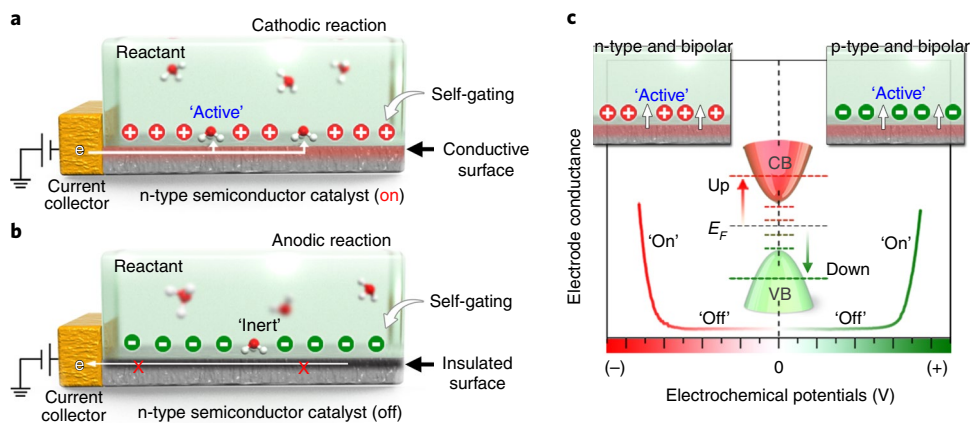


Fig. 4 | Correlation of the charge carrier type and the reaction in a semiconductor catalyst. **a, b**, Schematic of the effect of surface conductance on an n-type semiconductor catalyst for a cathodic reaction (**a**) and an anodic reaction (**b**). The self-gating turns on the surface of the n-type semiconductor (surface conductive) in a cathodic potential, facilitating electron transport and making the surface ‘active’ (**a**). In contrast, its surface is turned ‘off’ (surface insulated) at an anodic potential under self-gating (**b**), making the surface ‘inert’. **c**, Schematic of the correlation between the types of semiconductor and their preferred electrocatalytic activities. The n-type and bipolar semiconductors can be turned on by the negative electrochemical potential, making them suitable for cathodic reactions, while the p-type and bipolar semiconductors can be turned on by the positive electrochemical potential, and are thus suitable for anodic reactions.

Table 1 | Correlation between the charge carrier types of previously studied semiconductor catalysts and their preferred electrocatalytic reactions

Electronic properties		Preferred electrocatalytic reactions	
Charge carrier	Self-gating modulation	Semiconductor catalyst	Electrocatalytic reaction
n-type (electron)	'On' for negative electrochemical potentials	MoS ₂	HER and CO ₂ reduction
		MoSe ₂	HER
		WS ₂	HER
		WSe ₂	HER and CO ₂ reduction
		ZnO	CO ₂ reduction
		SnO ₂	CO ₂ reduction
		SnS ₂	HER
		ReS ₂	HER
		MoTe ₂	HER
		CoMoS _x	HER
p-type (hole)	'On' for positive electrochemical potentials	NiO	ORR and OER
		Ni(OH) ₂	OER
		CoO and Co ₃ O ₄	ORR and OER
		Co(OH) ₂	OER
		Cu ₂ O and CuO	ORR and OER
		Cu ₂ S	OER
		Mn ₃ O ₄	ORR and OER
		PtO ₂	OER
		NiCo ₂ O ₄	ORR and OER
		CuCo ₂ O ₄	ORR and OER
		MnCo ₂ O ₄	ORR and OER
		P-doped MoS ₂	ORR
		WSe ₂	ORR
WSe _{1.8} Te _{0.2}	OER		
Bipolar (electron and hole)	'On' for both	Ta- or Nb-doped MoS ₂	HER and ORR
		Ta- or Nb-doped WS ₂	HER and ORR
		WSe ₂	HER and OER

The corresponding literature is listed in Supplementary Table 4. Note: some metallic group VIA compounds, such as metal chalcogenides (for example, CoS₂, CoSe₂, NiS₂, NiCo₂S₄, VS₂, VTe₂, and PtTe₂) and metallic metal oxides (for example, RuO₂, RhO₂, IrO₂, PtCoO₂ and PdXO₂ [X = Co, Cr or Rh]) are not listed. For a detailed discussion see Supplementary Note 6.

as n-type, p-type and bipolar Si nanowires (Supplementary Fig. 25) and previously reported thin films, such as p-type Co_{1-x}Fe_xOOH (ref. 43) and Ni_{1-x}Fe_xOOH (ref. 44). It is worth mentioning that the efficient charge transport in semiconductors under self-gating is necessary for the electrocatalytic reaction to occur. On the other hand, the intrinsic catalytic activity of the semiconductor is another important factor that affects the charge transfer kinetics at the electrocatalytic reaction interface⁴⁵. Both contribute to the semiconductor electrocatalysis.

Table 1 summarizes the correlation between charge carrier types of the commonly used semiconductors and their preferred electrocatalytic reactions (HER, OER, CO₂ reduction or ORR). For example, n-type MX₂ (M = Mo, W, Re; X = S, Se) catalysts favour the HER, p-type Ni- and Co-based catalysts prefer the OER and ORR, and bipolar Ta/Nb-doped MoS₂ (or WS₂) catalysts tend to perform

both the HER and ORR (for detailed discussions see Supplementary Note 6). Our work provides a clear and comprehensive understanding of the semiconductor–electrolyte interface by bridging electrochemical activities with electronic states, and can further guide the rational design of semiconductor catalysts for various promising catalytic applications. Beyond electrocatalysis, the demonstration of self-gating can improve our understanding of a large variety of semiconductor–electrolyte interfaces in photoelectrochemical catalysis, photocatalysis, supercapacitors and batteries.

Online content

Any methods, additional references, Nature Research reporting summaries, source data, statements of code and data availability and associated accession codes are available at <https://doi.org/10.1038/s41563-019-0426-0>.

Received: 14 December 2018; Accepted: 5 June 2019;

Published online: 22 July 2019

References

- Allen, J. & Bard, L. R. F. *Electrochemical Methods: Fundamentals and Applications* 2nd edn (Wiley, 2000).
- Memming, R. *Semiconductor Electrochemistry* 2nd edn (Wiley, 2015).
- Rajeshwar, K. *Fundamentals of Semiconductor Electrochemistry and Photoelectrochemistry* Vol. 6 (Wiley, 2002).
- Nozik, A. J. & Memming, R. Physical chemistry of semiconductor–liquid interfaces. *J. Phys. Chem.* **100**, 13061–13078 (1996).
- Gao, Y. Q., Georgievskii, Y. & Marcus, R. A. On the theory of electron transfer reactions at semiconductor electrode/liquid interfaces. *J. Chem. Phys.* **112**, 3358–3369 (2000).
- Lewis, N. S. Progress in understanding electron-transfer reactions at semiconductor/liquid interfaces. *J. Phys. Chem. B* **102**, 4843–4855 (1998).
- Fajardo, A. M. & Lewis, N. S. Rate constants for charge transfer across semiconductor–liquid interfaces. *Science* **274**, 969–972 (1996).
- Marcus, R. A. On the theory of oxidation–reduction reactions involving electron transfer. I. *J. Chem. Phys.* **24**, 966–978 (1956).
- Gerischer, H. Charge transfer processes at semiconductor–electrolyte interfaces in connection with problems of catalysis. *Surf. Sci.* **18**, 97–122 (1969).
- Bisri, S. Z., Shimizu, S., Nakano, M. & Iwasa, Y. Endeavor of iontronics: from fundamentals to applications of ion-controlled electronics. *Adv. Mater.* **29**, 1607054 (2017).
- Du, H., Lin, X., Xu, Z. & Chu, D. Electric double-layer transistors: a review of recent progress. *J. Mater. Sci.* **50**, 5641–5673 (2015).
- Wang, Y. et al. Structural phase transition in monolayer MoTe₂ driven by electrostatic doping. *Nature* **550**, 487–491 (2017).
- Saito, Y., Kasahara, Y., Ye, J., Iwasa, Y. & Nojima, T. Metallic ground state in an ion-gated two-dimensional superconductor. *Science* **350**, 409–413 (2015).
- Vanmaekelbergh, D., Houtepen, A. J. & Kelly, J. J. Electrochemical gating: a method to tune and monitor the (opto)electronic properties of functional materials. *Electrochim. Acta* **53**, 1140–1149 (2007).
- Saito, Y. et al. Superconductivity protected by spin-valley locking in ion-gated MoS₂. *Nat. Phys.* **12**, 144–149 (2016).
- Ye, J. T. et al. Liquid-gated interface superconductivity on an atomically flat film. *Nat. Mater.* **9**, 125–128 (2010).
- Liu, L. et al. Probing the crystal plane effect of Co₃O₄ for enhanced electrocatalytic performance toward efficient overall water splitting. *ACS Appl. Mater. Interfaces* **9**, 27736–27744 (2017).
- Ling, T. et al. Engineering surface atomic structure of single-crystal cobalt (II) oxide nanorods for superior electrocatalysis. *Nat. Commun.* **7**, 12876 (2016).
- Yu, Y. et al. High phase-purity 1T'-MoS₂- and 1T'-MoSe₂-layered crystals. *Nat. Chem.* **10**, 638–643 (2018).
- Jaramillo, T. F. et al. Identification of active edge sites for electrochemical H₂ evolution from MoS₂ nanocatalysts. *Science* **317**, 100–102 (2007).
- Li, H. et al. Activating and optimizing MoS₂ basal planes for hydrogen evolution through the formation of strained sulphur vacancies. *Nat. Mater.* **15**, 48–53 (2016).
- Voiry, D., Yang, J. & Chhowalla, M. Recent strategies for improving the catalytic activity of 2D TMD nanosheets toward the hydrogen evolution reaction. *Adv. Mater.* **28**, 6197–6206 (2016).
- Franklin, A. D. *Electrocatalysis on Non-metallic Surfaces* (National Bureau of Standards, 1975).
- Ding, M. et al. An on-chip electrical transport spectroscopy approach for in situ monitoring electrochemical interfaces. *Nat. Commun.* **6**, 7867 (2015).

25. Ding, M. et al. Nanoelectronic investigation reveals the electrochemical basis of electrical conductivity in *Shewanella* and *Geobacter*. *ACS Nano* **10**, 9919–9926 (2016).
26. Zhang, Y. et al. Chemical vapor deposition of monolayer WS₂ nanosheets on Au foils toward direct application in hydrogen evolution. *Nano Res.* **8**, 2881–2890 (2015).
27. Fujimoto, T. & Awaga, K. Electric-double-layer field-effect transistors with ionic liquids. *Phys. Chem. Chem. Phys.* **15**, 8983–9006 (2013).
28. Chhowalla, M., Jena, D. & Zhang, H. Two-dimensional semiconductors for transistors. *Nat. Rev. Mater.* **1**, 16052 (2016).
29. DasA et al. Monitoring dopants by Raman scattering in an electrochemically top-gated graphene transistor. *Nat. Nanotechnol.* **3**, 210–215 (2008).
30. Braga, D., Gutiérrez Lezama, I., Berger, H. & Morpurgo, A. F. Quantitative determination of the band gap of WS₂ with ambipolar ionic liquid-gated transistors. *Nano Lett.* **12**, 5218–5223 (2012).
31. Ortiz, D. N. et al. Ambipolar transport in CVD grown MoSe₂ monolayer using an ionic liquid gel gate dielectric. *AIP Adv.* **8**, 035014 (2018).
32. Chen, X. et al. Probing the electron states and metal–insulator transition mechanisms in molybdenum disulfide vertical heterostructures. *Nat. Commun.* **6**, 6088 (2015).
33. Chu, L. et al. Charge transport in ion-gated mono-, bi- and trilayer MoS₂ field effect transistors. *Sci. Rep.* **4**, 7293 (2014).
34. Xia, J., Chen, F., Li, J. & Tao, N. Measurement of the quantum capacitance of graphene. *Nat. Nanotechnol.* **4**, 505–509 (2009).
35. Lezama, I. G. et al. Single-crystal organic charge-transfer interfaces probed using Schottky-gated heterostructures. *Nat. Mater.* **11**, 788 (2012).
36. Kaji, T., Takenobu, T., Morpurgo, A. F. & Iwasa, Y. Organic single-crystal Schottky gate transistors. *Adv. Mater.* **21**, 3689–3693 (2009).
37. Neamen, D. *Semiconductor Physics and Devices* (McGraw-Hill, 2003).
38. Xu, Z. J. From two-phase to three-phase: the new electrochemical interface by oxide electrocatalysts. *Nano-Micro Lett.* **10**, 8 (2017).
39. Suntivich, J., May, K. J., Gasteiger, H. A., Goodenough, J. B. & Shao-Horn, Y. A perovskite oxide optimized for oxygen evolution catalysis from molecular orbital principles. *Science* **334**, 1383–1385 (2011).
40. Liang, Y. et al. Co₃O₄ nanocrystals on graphene as a synergistic catalyst for oxygen reduction reaction. *Nat. Mater.* **10**, 780–786 (2011).
41. Wei, C. et al. Cations in octahedral sites: a descriptor for oxygen electrocatalysis on transition-metal spinels. *Adv. Mater.* **29**, 1606800 (2017).
42. Liu, Y. et al. Self-optimizing, highly surface-active layered metal dichalcogenide catalysts for hydrogen evolution. *Nat. Energy* **2**, 17127 (2017).
43. Burke, M. S., Kast, M. G., Trotochaud, L., Smith, A. M. & Boettcher, S. W. Cobalt-iron (oxy)hydroxide oxygen evolution electrocatalysts: the role of structure and composition on activity, stability and mechanism. *J. Am. Chem. Soc.* **137**, 3638–3648 (2015).
44. Trotochaud, L., Young, S. L., Ranney, J. K. & Boettcher, S. W. Nickel-iron oxyhydroxide oxygen-evolution electrocatalysts: the role of intentional and incidental iron incorporation. *J. Am. Chem. Soc.* **136**, 6744–6753 (2014).
45. Seh, Z. W. et al. Combining theory and experiment in electrocatalysis: insights into materials design. *Science* **355**, eaad4998 (2017).

Acknowledgements

This work was supported by MOE under AcRF Tier 1 (M4011782.070 RG4/17 and M4011993.070 RG7/18), AcRF Tier 2 (2015-T2-2-007, 2016-T2-1-131, 2016-T2-2-153 and 2017-T2-2-136) and AcRF Tier 3 (2018-T3-1-002), and the A*Star QTE programme. This work was also supported by MOE under AcRF Tier 1 (2016-T1-002-051, 2017-T1-001-150 and 2017-T1-002-119) and AcRF Tier 2 (2015-T2-2-057, 2016-T2-2-103 and 2017-T2-1-162), and by NTU under Start-Up Grant M4081296.070.500000 in Singapore. H.Z. acknowledges support from ITC via the Hong Kong Branch of National Precious Metals Material Engineering Research Center and a Start-Up Grant from City University of Hong Kong. The authors acknowledge the Facility for Analysis, Characterization, Testing and Simulation, Nanyang Technological University, Singapore for use of their electron microscopy facilities. Q.J.W. acknowledges the support of the Ministry of Education Singapore Grant (MOE2016-T2-1-128) and National Research Foundation–Competitive Research Program (NRF-CRP18-2017-02). Z.Z. acknowledges the support from NSFC (11772153). Z.W.S. acknowledges support from the Institute of Materials Research and Engineering, A*STAR (IMRE/17-1R1211). Work at Rice was supported by the US ARO Grant W911NF-16-1-0255. The authors thank Z.J. Xu for discussions about surface conductance and L. Han, J.R. Galan-Mascaros (Institute of Chemical Research of Catalonia) and P. Tang (Catalonia Institute for Energy Research) for discussions about EIS. The authors also thank Y. Liu (Hunan University) for discussions about the semiconductor electronic device and S. Teddy for XPS measurements and data analysis.

Author contributions

H.Z. and Z.L. guided the project. Y.H. and Q.H. observed the self-gating phenomenon, designed the experiments, fabricated the devices and performed in situ electrochemical and EIS measurements and analysis. Q.H., Y.H., M.D., C.Z. and S.G. made the microcell set-up. Lu.W., Z.Z. and B.I.Y. performed the first-principle calculations and analysed the simulation data. Y.H., P.G., C.G. and X.W. synthesized single-layer TMD nanosheets. P.Y., Q.Z., F.L., Li.W. and M.W. synthesized TMD crystals. X.Y. synthesized Si nanowires. Z.X., A.D.H. and Z.W.S. analysed the electrochemical results and revised the manuscript. Y.H., Q.H., H.Z. and Z.L. conceived and supervised the experiments. Y.H., Q.H., Q.J.W., H.Z. and Z.L. wrote the paper. All authors discussed the results and commented on the manuscript.

Competing interests

The authors declare no competing interests.

Additional information

Supplementary information is available for this paper at <https://doi.org/10.1038/s41563-019-0426-0>.

Reprints and permissions information is available at www.nature.com/reprints.

Correspondence and requests for materials should be addressed to Q.J.W., H.Z. or Z.L.

Publisher's note: Springer Nature remains neutral with regard to jurisdictional claims in published maps and institutional affiliations.

© The Author(s), under exclusive licence to Springer Nature Limited 2019

Methods

Growth of single-layer WS₂. Chemical vapour deposition (CVD) was used to grow single-layer WS₂ with halide-assisted atmospheric pressure growth⁴⁶. A mixture of WO₃ and NaCl (referred to as WO₃/NaCl) and S powders as precursors were placed in the centre and upstream of the tube furnace, respectively. Excess S was supplied so that the vapour was sufficient for large-area growth of WS₂. High-purity Ar served as the carrier gas and a clean SiO₂ (285 nm)/Si wafer was used as the growth substrate, which was placed face down on top of the WO₃/NaCl (8:1 mass ratio). Before the growth process, the tube furnace was thoroughly purged with Ar (500 s.c.c.m.) for 10 min to remove the trace amounts of air. The growth temperature was kept at 750–820 °C under 50 s.c.c.m. Ar flow at atmospheric pressure, while the S powder was kept at ~160 °C. After growth for 10–15 min, the furnace was naturally cooled to room temperature.

Introduction of four types of microcell. Four types of microcell were developed in our work, as shown in Supplementary Fig. 1: type 1, a microcell for in situ electronic/electrochemical measurements, which can simultaneously collect the electronic and electrochemical signals of semiconductor electrocatalysts in a large potential window; type 2, a microcell for thickness-dependent electrocatalytic measurements, which can examine the HER performance of MoS₂ of various thicknesses (1–101 nm) to obtain the penetration depth of the surface conductance (in this microcell, the electrochemical current transports vertically through the semiconductor to the bottom electrode); type 3, a microcell for top and bottom electrode measurements, which can investigate the surface and bulk conductance of the semiconductor flake; type 4, a microcell for photoelectrochemical measurements, which can measure not only the photoconductance and photoelectrochemical current simultaneously, but also the photoresponse time at various electrochemical potentials.

Fabrication of microcells for in situ electronic/electrochemical measurements.

A typical fabrication procedure is shown in Supplementary Fig. 2. First, a 16 × 16 mm² SiO₂ (285 nm)/Si chip with 32 prepatterned Au contact pads was fabricated using conventional photolithography. CVD-grown single-layer WS₂ (left, Supplementary Fig. 2) or mechanically exfoliated TMDs (MoS₂, WSe₂, WSe_{1.8}Te_{0.2} (ref. 47), ReSe₂, PtSe₂ and MoTe₂) nanosheets (right, Supplementary Fig. 2) were transferred onto the chips. The mechanically exfoliated TMD nanosheets were treated with Ar plasma (3 W at 6.5 × 10⁻³ torr for 15 s) to create S, Se or Te vacancies (2–4%) to provide more active sites²¹. Electron-beam lithography, followed by thermal or electron-beam evaporation, were then used to fabricate metal contacts for the drain and source, which contacted the Au pads on the chip (metal contacts: Cr (5 nm)/Au (60 nm) for MoS₂, ReS₂ and single-layer WS₂; Pd (5 nm)/Au (60 nm) for WSe_{1.8}Te_{0.2}; Ti (5 nm)/Au (60 nm) for WSe₂, PtSe₂ and MoTe₂). Finally, the device chip was passivated with 1-μm-thick PMMA film, followed by the electron-beam lithography process to open a window through the PMMA to expose the region of interest on the nanosheet.

As a control experiment, a Pt microelectrode was fabricated onto the chip by laser writing followed by electron-beam evaporation of 40 nm Pt. Subsequent processes were similar to those used for fabrication of the microcells.

Fabrication of microcells for top and bottom electrode measurements.

A typical fabrication procedure for a microcell with top and bottom electrodes is shown in Supplementary Fig. 21. Two bottom electrodes (Cr/Au, 2 nm/15 nm) were first fabricated to contact the Au contact pads by electron-beam lithography, followed by thermal evaporation. Second, a MoS₂ nanosheet with thickness of 20–40 nm was mechanically exfoliated onto PDMS and then dry transferred onto the targeted bottom electrode. Third, two top electrodes (Ti/Au, 2 nm/80 nm) were fabricated on the MoS₂ nanosheet, which were vertically aligned to the bottom electrode (without direct contact) by electron-beam lithography followed by thermal evaporation. Fourth, S vacancies (~10%) were introduced in MoS₂ by Ar plasma (3 W for 45 s at 6.5 × 10⁻³ torr) to increase the number of active sites. The devices were then passivated with 1-μm-thick PMMA film, followed by electron-beam lithography to open a reaction window on the basal plane of the MoS₂ while avoiding the exposure of edges and electrodes. Devices with in-plane top and bottom electrodes (Supplementary Figs. 21–24b) were also tested in our experiment, and were found to behave in a similar manner to the vertically aligned ones.

Fabrication of microcells for thickness-dependent electrocatalytic measurements.

A typical fabrication procedure for microcells with different thicknesses (1–100 nm) of MoS₂ nanosheets is shown in Supplementary Fig. 22. Briefly, both CVD-grown single-layer MoS₂ and mechanically exfoliated multilayer MoS₂ nanosheets were transferred onto Au contacts on SiO₂/Si chips. S vacancies (~10 %) were then introduced into the MoS₂ by Ar plasma (3 W, 45 s) to increase the number of active sites. Atomic force microscopy (AFM) was used to confirm the thickness of the MoS₂ nanosheets. Finally, all devices were passivated with 1-μm-thick PMMA film, followed by electron-beam lithography to open reaction windows on the basal planes of the MoS₂.

Fabrication of Si nanowire-based microcell devices. Si nanowires were fabricated by chemical etching of light-doped Si wafers⁴⁸ (doping concentration ~10¹³ e cm⁻³). The as-fabricated Si nanowires could be easily removed from the wafer surface,

resulting in a homogeneous suspension in isopropyl alcohol through low-power sonication. The Si nanowires were then dropcast onto pre-patterned chips with Au contact pads, which showed a broad distribution of diameters (50–300 nm) and lengths (10–20 μm). By using transmission electron microscopy, porous structures were observed on the surface of the Si nanowires. Their edge-rich characteristic may provide active sites for the electrocatalysis. The device fabrication procedure is similar to that used for TMD microcells, except for the thicker metal electrode (Cr/Au, 5 nm/200 nm).

In situ electronic/electrochemical measurements in microcells. A microcell was appropriately set up to study the surface charge injection⁴⁹ and charge transfer processes⁵⁰ in a more controlled manner. Here, the in situ electronic/electrochemical measurements were conducted in a droplet of 0.5 M H₂SO₄ electrolyte in a microcell.

There are four electrodes in the microcell. Two are connected to a graphite and a Ag/AgCl micro reference electrode (Harvard Apparatus), used as the counter and references, respectively. The other two electrodes are connected to the TMD nanosheet as drain and source contacts to collect their electronic signals during electrocatalysis. In all experiments, only the exposed region of the nanosheet contributes to the electrocatalytic performance, and the rest of the area in contact with the electrolyte is passivated with PMMA. During the HER (−0.4 V versus RHE), a H₂ microbubble was only observed on top of the exposed MoS₂ surface, indicating that the electrochemical reaction only occurs in the reaction window (Supplementary Fig. 3). Before the electrocatalytic measurements on the TMD nanosheets, the fabricated Pt microelectrode in the reaction window (Supplementary Fig. 4a) was tested. The Pt microelectrode shows a Tafel slope of 37.2 mV dec⁻¹ and onset potential less than 10 mV (Supplementary Fig. 4b,c), consistent with reported results²¹, proving that our microcell set-up is suitable for the electrocatalytic reaction.

Representative data on n-type MoS₂ and bipolar WSe₂ nanosheets were collected during the in situ electronic/electrochemical measurements (Supplementary Fig. 5). The scan rate of the electrochemical potential is 5 mV per step, and the scan direction is as follows: zero → cathodic (HER) → zero → anodic (OER) → zero. The electronic (I_{ds}) and electrochemical (I_c) signals were recorded simultaneously. Normally, I_{ds} is ~10–1,000 times I_c in our experiment, which is dependent on the conductance of the semiconductor catalyst and the bias voltage (V_{ds}). The electrochemical current density was calculated by normalizing the current to the open area of PMMA on the TMD nanosheets. In this work, we express the electrochemical reference voltage with respect to RHE:

$$E_{\text{RHE}} = E_{\text{Ag/AgCl}} + 0.219 \text{ V}$$

EIS measurement in microcells. The EIS measurements were performed on the MoS₂ nanosheet and Au microelectrodes in the respective microcells at various electrochemical potentials from −0.14 to −0.38 V (versus RHE), during HER, by using an Autolab PGSTAT204 in the frequency range 10²–10⁵ Hz with an amplitude of 10 mV. Data fitting was conducted on the basis of a Randles equivalent circuit model, employing constant phase element (Q element, CPE) using Nova 2.1.2 software. Because I_c is very low in the micro-electrochemical set-up (on the order of 10⁻⁸–10⁻⁷ A), no gas bubble was observed during EIS measurements. For each MoS₂ nanosheet microelectrode, the in situ electronic/electrochemical measurement was conducted on the same device to compare the charge transport resistance with the value extracted from EIS measurements.

Material characterizations. The TMDs were characterized by optical microscopy, AFM (Bruker 8 AFM microscope system in ScanAsyst mode), scanning electron microscopy (FEI 4200) and Raman spectroscopy (WITec alpha300 R) performed with a 532 nm laser (with a spot size ~500 nm in diameter) at room temperature. The in situ electronic/electrochemical measurements were performed by combining two source meters (Keithley 2400 and 2450).

Data availability

The data that support the findings of this study are available from the corresponding author on reasonable request.

References

- Li, S. et al. Halide-assisted atmospheric pressure growth of large WSe₂ and WS₂ monolayer crystals. *Appl. Mater. Today* **1**, 60–66 (2015).
- Huang, J.-H. et al. Large-area 2D layered MoTe₂ by physical vapor deposition and solid-phase crystallization in a tellurium-free atmosphere. *Adv. Mater. Interfaces* **4**, 1700157 (2017).
- Salvatierra Rodrigo, V. et al. Silicon nanowires and lithium cobalt oxide nanowires in graphene nanoribbon papers for full lithium ion battery. *Adv. Energy Mater.* **6**, 1600918 (2016).
- Voiry, D. et al. The role of electronic coupling between substrate and 2D MoS₂ nanosheets in electrocatalytic production of hydrogen. *Nat. Mater.* **15**, 1003–1009 (2016).
- Wang, J. et al. Field effect enhanced hydrogen evolution reaction of MoS₂ nanosheets. *Adv. Mater.* **29**, 1604464 (2017).